The Twin Array and Its Higher-Order Arrangements: A Novel Approach to DOF Enhancement via New Spatial Domains

Ahmed M. A. Shaalan, *Member, IEEE*, and AbdulGuddoos S. A. Gaid, *Member, IEEE*

***Abstract*—This paper presents a novel approach for enhancing the degrees of freedom (DOF) of a physical sensor array by generating new spatial domains. The technique begins by applying a Qth-order Hadamard product to the output vector of the physical sensor array, which generates a virtual output vector characterized by a unique Qth-order steering vector. This steering vector, in turn, defines a virtual Qth-order twin array. The output vector of this twin array is then utilized to extend the original array output, forming an extended covariance matrix that incorporates three distinct domains for spatial analysis: the physical array domain, the twin array domain, and the cross domain between them. A theorem, grounded in the logic of the standard multinomial theorem, is introduced to define the properties of this new configuration, and the performance of the extended output vector is thoroughly evaluated and compared against the original using direction of arrival (DOA) estimation. Finally, extensive simulation results demonstrate the enhancement in uniform DOF achieved by the proposed approach.**

***Index Terms*—Sensor arrays, Qth-order twin arrays, Qth-order Hadamard product, degree of freedom (DOF), complex Gaussian signals (CGSs), direction of arrival (DOA) estimation.**

I. Introduction

In sensor array design and processing, different from uniform linear arrays (ULAs) [1], which establish a linear relationship between the physical sensors and the uniform degrees of freedom (DOF) resulting from the pairwise differences in the physical sensor locations, nested arrays (NAs) [2] and co-prime arrays (CPAs) [3], [4] have emerged as a novel approach to array signal processing with enhanced DOF. Instead of maintaining uniform spacing among all sensors, these structures segment the array into smaller sub-arrays with different inter-sensor spacings. This configuration reduces the redundancy in generating the same pairwise differences, thereby increasing the uniform DOF.

Consequently, NAs and CPAs have laid the groundwork for various nonuniform arrays over the last decade [5]–[21]. For example, the enhanced and generalized co-prime array (EGCA) [11] has enhanced the uniform DOF of the CPA. Similarly, the super augmented nested arrays (SANA) [13] have augmented the uniform DOF of the NA. However, specific arrays, namely the super dilated nested array (SDNA) [15], [16], and the improved co-prime nested array (ICNA) [17] have successfully combined the high uniform DOF of the NA with the low weight function of the CPA.

The authors are with the Faculty of Engineering and Information Technology, Taiz University, Taiz, Yemen (shaalan.ahmed@taiz.edu.ye; quddoos.gaid@taiz.edu.ye).

Manuscript received April 19, 2021; revised August 16, 2021.

However, the degree of freedom is determined by the number of distinct pairwise differences, aka "virtual sensors," in the difference array. Therefore, repositioning the physical sensors to maximize the uniform DOF is crucial and has been the typical design goal for these arrays [5]–[21]. Although these arrays can indeed estimate more sources than physical sensors, they only utilize the difference array. Consequently, arrays, considering the sum array as another domain, similar to the difference array, have been developed [22]–[29]. Furthermore, to enhance the uniform DOF even further, various geometries based on high-order cumulants have recently been introduced [30]–[40].

In this paper, we present a novel approach to array signal processing that enhances the DOF by moving beyond the single baseline domain of a physical sensor array and introducing new spatial domains. Our method is motivated by viewing the sensor output as a weighted sum of base components from the arriving signals. By raising this sum to an integer power Q, we generate a Qth-order expansion comprising harmonic and cross terms of these signals. The harmonic terms correspond to a new virtual sensor location (Qp_i, where p_i is the physical sensor location), which measures the Qth-order instantaneous amplitudes of the incoming signals. In contrast, the cross-signal terms represent interference resulting from signal mixing. These measurements are also contaminated by the Qth-order sensor noise and unwanted cross terms between the noise and the received signals.

Nevertheless, the expanded observations are assembled into a vector characterized by a unique Qth-order steering vector derived from the original. We refer to this assembled vector as the output of a "Qth-order twin array" and exploit it to extend the physical array output, thereby forming an extended array covariance matrix. This new matrix incorporates additional spatial domains beyond the original domain of the physical array: specifically, the domain of the Qth-order twin array and the cross domain between the physical array and its twin. Furthermore, we demonstrate that although the twin array is constructed via a nonlinear operation, the Qth-order moment of its output does not adversely affect the extended covariance matrix structure. This is because the second-order moment, representing the signal power, remains the dominant component. Consequently, standard second-order, subspace-based direction of arrival (DOA) estimation algorithms can be applied effectively.

This paper is organized as follows. Section II presents the sparse array signal processing model, which serves as the

foundation for the array model developed in Section III. The core of the theoretical contribution for this study is presented in Section III. Specifically, Section III-A introduces Theorem 1, which explains how the virtual Qth-order twin array output vector is derived from the output vector of the physical sensor array via the Qth-order Hadamard product. The theorem defines the general forms of the resulting harmonic and cross terms, enumerates the distinct terms in each form, and establishes the multiplicities of these distinct terms within the polynomial.

Building on this generalized closed-form expression, Section III-B introduces a new array signal model that incorporates the twin array output vector. It also derives the expected value of each term type within this output vector — including signal-cross and signal-noise cross terms for an arbitrary order Q — and presents the specific form of the extended array covariance matrix for circular signals, particularly complex Gaussian signals.

Section IV discusses and compares the physical array output with the combined output of the physical and twin arrays. It then examines how Qth-order twin array components — such as harmonic-signal terms, the harmonic-noise term, and interference terms (signal-cross and signal-noise cross terms) — affect the extended-array covariance matrix and, in turn, the performance of subspace-based DOA estimation algorithms. Section V presents simulation results validating the enhanced DOF capacity achieved by the physical-virtual array structure. Finally, Section VI provides concluding remarks.

The following notations are adopted throughout this paper: boldface lower-case letters (e.g., $\mathbf{a}$) denote vectors, boldface upper-case letters (e.g., $\mathbf{A}$) denote matrices, and outlined letters (e.g., $\mathbb{P}$, $\mathbb{D}$) denote sets. The operators $()^*$, $()^\top$, and $()^H$ represent complex conjugation, transpose, and Hermitian (complex conjugate transpose), respectively. The notation $(\cdot)^{\circ Q}$ signifies the Qth-order element-wise (Hadamard) power. The $\mathrm{vec}(\cdot)$ operator vectorizes a matrix by stacking its columns. The symbols $\otimes$ and $\circ$ represent the Kronecker and Hadamard products, respectively. Finally, $\mathrm{diag}(\mathbf{A})$ denotes a matrix formed by retaining only the diagonal elements of $\mathbf{A}$, with all off-diagonal elements set to zero.

II. Sparse Array Signal Processing

Assume K narrow-band far-field uncorrelated signals with complex amplitudes $[s_1(t), \ldots, s_K(t)]$, modeled as random variables following complex Gaussian distributions ($\mathcal{CN}(0, \sigma_k^2)$). Their angles of arrival $[\theta_1, \ldots, \theta_K]$ lie within the range $[-\pi/2, \pi/2]$. These signals are intercepted by a sparse linear array composed of N physical sensors. The sensors are located at positions given by the set $\mathbb{P} = \{p_1, \ldots, p_N\}$, where each position is a multiple of a fundamental distance d: $p_i = p_i d$ for $i = 1, \ldots, N$. The parameter d, denoting the minimum inter-sensor spacing, is half the wavelength, $d = \lambda/2$. Then, the physical array output vector at time instant t (for $t = 1, \ldots, T$) can be modeled as

$$\mathbf{x}_{\mathbb{P}}(t) = \sum_{k=1}^{K} \mathbf{a}_{\mathbb{P}}(\theta_k) s_k(t) + \mathbf{n}_{\mathbb{P}}(t) = \mathbf{A}_{\mathbb{P}} \mathbf{s}_{\mathbb{P}}(t) + \mathbf{n}_{\mathbb{P}}(t), \quad (1)$$

where

$$\mathbf{a}_{\mathbb{P}}(\theta_k) = \left[e^{j2\pi(p_1 d/\lambda)\sin(\theta_k)}, \quad \ldots, \quad e^{j2\pi(p_N d/\lambda)\sin(\theta_k)} \right]^\top \quad (2)$$

is the array steering vector for the kth signal direction θ_k, $\mathbf{A}_{\mathbb{P}} = [\mathbf{a}_{\mathbb{P}}(\theta_1), \ldots, \mathbf{a}_{\mathbb{P}}(\theta_K)]$ is the array manifold matrix of size $N \times K$, $\mathbf{s}_{\mathbb{P}}(t) = [s_1(t), \ldots, s_K(t)]^\top$ is the source signal vector, and $\mathbf{n}_{\mathbb{P}}(t) = [n_1(t), \ldots, n_N(t)]^\top$ is an additive white Gaussian noise vector with i.i.d. components distributed as $\mathcal{CN}(0, \sigma_n^2)$.

The primary process in array processing, which involves computing the array spatial covariance matrix $\mathbf{R}_{\mathbb{PP}}$ by applying the statistical expectation operator $E[\cdot]$ to the product of $\mathbf{x}_{\mathbb{P}}(t)$ with its Hermitian, is given by

$$\mathbf{R}_{\mathbb{PP}} = E[\mathbf{x}_{\mathbb{P}}(t)\mathbf{x}_{\mathbb{P}}^H(t)] = \mathbf{A}_{\mathbb{P}} \mathbf{R}_{\mathbf{ss}} \mathbf{A}_{\mathbb{P}}^H + \mathbf{R}_{\mathbf{nn}}, \quad (3)$$

where $\mathbf{R}_{\mathbf{ss}} = E[\mathbf{s}_{\mathbb{P}}(t)\mathbf{s}_{\mathbb{P}}^H(t)]$ and $\mathbf{R}_{\mathbf{nn}} = E[\mathbf{n}_{\mathbb{P}}(t)\mathbf{n}_{\mathbb{P}}^H(t)]$ represent the covariance matrices of the source signals and noise, respectively. Since the arriving signals are assumed to be uncorrelated, $\mathbf{R}_{\mathbf{ss}}$ is a diagonal matrix, such that its main diagonal $\mathbf{r}_{\mathbf{ss}} = \mathrm{diag}(\mathbf{R}_{\mathbf{ss}}) = [\sigma_1^2, \ldots, \sigma_K^2]$ is the signal power vector. Therefore, (3) can be expressed as

$$\begin{aligned} \mathbf{R}_{\mathbb{PP}} &= \sum_{k=1}^{K} \sigma_k^2 (\mathbf{a}_{\mathbb{P}}(\theta_k)\mathbf{a}_{\mathbb{P}}^H(\theta_k)) + \sigma_n^2 \mathbf{I}_N \\ &= \sum_{k=1}^{K} \sigma_k^2 \mathbf{D}_{\mathbb{P}}(\theta_k) + \sigma_n^2 \mathbf{I}_N, \end{aligned} \quad (4)$$

where $\mathbf{I}_N$ is an $N \times N$ identity matrix, and $\mathbf{D}_{\mathbb{P}}(\theta_k)$ of size $N \times N$ — resulting from the product of the steering vector with its Hermitian — is a new steering matrix. The elements of $\mathbf{D}_{\mathbb{P}}(\theta_k)$ are of the form $e^{j2\pi(p_i - p_j)(d/\lambda)\sin(\theta_k)}$ for $i, j = 1, \ldots, N$. This corresponds to a new set of virtual sensor locations given by the pairwise differences of the physical sensor positions, $\mathbb{D}_{\mathbb{P}} = \{\tilde{p}_l = p_i - p_j : p_i, p_j \in \mathbb{P},\, l = 1, \ldots, N^2\}$.

As such, to create a virtual steering vector corresponding to the N^2 virtual sensor locations for the kth signal direction, the matrix $\mathbf{D}_{\mathbb{P}}(\theta_k)$ is vectorized into $\mathbf{d}_{\mathbb{P}}(\theta_k)$. Consequently, the vectorized covariance matrix is given by

$$\mathbf{r}_{\mathbb{PP}} = \mathrm{vec}(\mathbf{R}_{\mathbb{PP}}) = \sum_{k=1}^{K} \sigma_k^2 \mathbf{d}_{\mathbb{P}}(\theta_k) + \sigma_n^2 \mathbf{1}, \quad (5)$$

where $\mathbf{1}$ is the vectorized form of the identity matrix $\mathbf{I}_N$ (i.e., $\mathbf{1} = \mathrm{vec}(\mathbf{I}_N)$), and the virtual steering vector $\mathbf{d}_{\mathbb{P}}(\theta_k)$ can be expressed more insightfully using the Kronecker product as

$$\begin{aligned} \mathbf{d}_{\mathbb{P}}(\theta_k) &= \mathrm{vec}(\mathbf{D}_{\mathbb{P}}(\theta_k)) = \mathrm{vec}(\mathbf{a}_{\mathbb{P}}(\theta_k)\mathbf{a}_{\mathbb{P}}^H(\theta_k)) \\ &= \mathbf{a}_{\mathbb{P}}^*(\theta_k) \otimes \mathbf{a}_{\mathbb{P}}(\theta_k) \in \mathbb{C}^{N^2 \times 1}, \text{ so that} \\ \mathbf{d}_{\mathbb{P}}(\theta_k) &= [e^{j2\pi\tilde{p}_1(d/\lambda)\sin(\theta_k)}, \ldots, e^{j2\pi\tilde{p}_{N^2}(d/\lambda)\sin(\theta_k)}]^\top. \end{aligned} \quad (6)$$

However, the N^2 virtual sensor locations in $\mathbb{D}_{\mathbb{P}}$ (corresponding to the entries of $\mathbf{r}_{\mathbb{PP}}$) are not unique and may not be consecutive. Therefore, a processed data vector $\mathbf{r}_{\mathbb{U}}$, corresponding to a central ULA segment $\mathbb{U}$ composed of the consecutive virtual sensor locations at the center of $\mathbb{D}_{\mathbb{P}}$, is

obtained by averaging the correlation statistics from redundant physical sensor pairs as

$$\mathbf{r}_{\mathbb{U}} = \frac{1}{w(\tilde{p}_i)} \sum_{\tilde{p}=-\tilde{p}_{\mathbb{U}}}^{\tilde{p}_{\mathbb{U}}} \langle \mathbf{r}_{\mathbb{P}\mathbb{P}} \rangle_{\tilde{p}_i}, \tag{7}$$

where the angle brackets denotes the received signal at the virtual sensor location $\tilde{p} = p_i - p_j$, and $\pm\tilde{p}_{\mathbb{U}}$ are the virtual sensor locations bounding $\mathbb{U}$ on the positive and negative sides, and $w(\tilde{p})$ obtained as $w(\tilde{p}) = \{(p_i, p_j) \in \mathbb{P} \mid p_i - p_j = \tilde{p}_l\}$ is the weight (or redundancy) of the virtual sensor location $\tilde{p}_l$, indicating the number of physical sensor pairs that contribute to it.

In summary, for a sparse array with the sensor location set $\mathbb{P}$, its difference array is $\mathbb{D}_{\mathbb{P}}$. If a second sensor location set $\mathbb{T}_Q$ is included to form a combined array, the overall virtual difference array is the union of the self-difference sets of each individual array and the cross-difference set between them; i.e.,

$$\mathbb{D}_{\text{all}} = \mathbb{D}_{\mathbb{P}} \cup \mathbb{D}_{\mathbb{T}_Q} \cup \mathbb{D}_{\mathbb{P},\mathbb{T}_Q} \cup \mathbb{D}_{\mathbb{T}_Q,\mathbb{P}}, \tag{8}$$

where $\mathbb{D}_{\mathbb{T}_Q} = \{\tau_i - \tau_j : \forall \tau_i, \tau_j \in \mathbb{T}_Q\}$ is the self-difference array of $\mathbb{T}_Q$ and the cross-difference set $\mathbb{D}_{\mathbb{T}_Q\mathbb{P}}$ is defined as

$$\mathbb{D}_{\mathbb{T}_Q\mathbb{P}} = \text{diff}(\mathbb{T}_Q, \mathbb{P}) = \{\tau - p \mid \forall \tau \in \mathbb{T}_Q, \forall p \in \mathbb{P}\}, \tag{9}$$

bearing in mind that $\mathbb{D}_{\mathbb{P}\mathbb{T}_Q} = -\mathbb{D}_{\mathbb{T}_Q\mathbb{P}}$. The cardinality of the difference array $\mathbb{D}_{\text{all}}$ represents the total number of unique DOF offered by the combined array. In contrast, the cardinality of $\mathbb{U}$ represents the number of uniform DOF, where $\tilde{p}_{\mathbb{U}}$ is the one-sided number of uniform DOF.

In practice, the array covariance matrix in (3) is estimated using the time-averaging operator of the available T time snapshots, i.e.,

$$\hat{\mathbf{R}}_{\mathbb{P}\mathbb{P}} = \frac{1}{T} \sum_{t=1}^{T} \mathbf{x}_{\mathbb{P}}(t) \mathbf{x}_{\mathbb{P}}^H(t). \tag{10}$$

III. QTH-ORDER TWIN ARRAY

A. Concept of the Qth-Order Twin Array

This subsection details the formulation of the Qth-order twin array, which is constructed based on the logic of the multinomial theorem.

Theorem 1 (The Qth-order Twin Array): Let $\mathbf{x}_{\mathbb{P}}(t)$ be the output vector of a physical sensor array with sensor location set $\mathbb{P}$, the Qth-order Hadamard power of the output vector, $(\mathbf{x}_{\mathbb{P}}(t))^{\circ Q}$, is equivalent to the output vector of a virtual sensor array, whose steering vector corresponds to a sensor location set $\mathbb{T}_Q$ given by $\mathbb{T}_Q = Q\mathbb{P} = \{Qp_i \mid p_i \in \mathbb{P}\}$.

Proof: For a physical sensor array, the sensor output is a weighted sum of the signals from all directions of arrival ($\left[\sum_{k=1}^{K} s_k(t)\mathbf{a}(\theta_k)\right]_i$). Raising that element to the power Q follows the logic of the standard multinomial theorem [41], [42]. This theorem states that raising a finite sum of terms to a non-negative integer power is equivalent to summing over all possible combinations of non-negative integer exponents that add up to that power. Explicitly, the expansion of a sum of K base terms (s_k) raised to power Q is

$$(s_1 + s_2 + ... + s_K)^Q = \sum \frac{Q!}{r_1! r_2! \dots r_K!} \prod_{k=1}^{K} s_k^{r_k}, \tag{11}$$

for all $r_k \geq 0$ such that $r_1 + r_2 + \cdots + r_K = Q$. To apply this logic to a vector, we treat each of its elements — each representing a sensor in the array — individually.

Assume that $\mathbf{x}_{\mathbb{P}}(t)$ represents the signal with no noise component; that is, $\mathbf{x}_{\mathbb{P}}(t) = \sum_{k=1}^{K} s_k(t)\mathbf{a}_{\mathbb{P}}(\theta_k)$. Then, consider the i-th element of this vector, where $i = 1, 2, \dots, N$. That is,

$$[\mathbf{x}_{\mathbb{P}}(t)]_i = \sum_{k=1}^{K} s_k(t)[\mathbf{a}_{\mathbb{P}}(\theta_k)]_i, \tag{12}$$

where $[\cdot]_i$ denotes the i-th element of the vector. Raising this vector to the Hadamard power Q means raising each of its individual elements to the power Q. Specifically,

$$[(\mathbf{x}_{\mathbb{P}}(t))^{\circ Q}]_i = \left(\sum_{k=1}^{K} s_k(t)[\mathbf{a}_{\mathbb{P}}(\theta_k)]_i \right)^Q. \tag{13}$$

In (13), we have a sum of scalars (not vectors). Therefore, the multinomial theorem formulation can directly be applied to this scalar as

$$[(\mathbf{x}_{\mathbb{P}}(t))^{\circ Q}]_i = \sum_{\substack{r_k \geq 0 \\ \sum r_k = Q}} \frac{Q!}{r_1! r_2! \dots r_K!} \prod_{k=1}^{K} \left(s_k(t)[\mathbf{a}_{\mathbb{P}}(\theta_k)]_i\right)^{r_k}. \tag{14}$$

Now, since $[(\mathbf{u})^{\circ r}]_i = [\mathbf{u}]_i^r$ and $[\mathbf{u} \circ \mathbf{v}]_i = [\mathbf{u}]_i[\mathbf{v}]_i$, $\prod_{k=1}^{K} [\mathbf{a}_{\mathbb{P}}(\theta_k)]_i^{r_k} = [(\mathbf{a}_{\mathbb{P}}(\theta_1))^{\circ r_1} \circ (\mathbf{a}_{\mathbb{P}}(\theta_2))^{\circ r_2} \circ \cdots \circ (\mathbf{a}_{\mathbb{P}}(\theta_K))^{\circ r_K}]_i$. Thereby, the complete vector can be written as

$$(\mathbf{x}_{\mathbb{P}}(t))^{\circ Q} = \sum_{\substack{r_k \geq 0 \\ \sum r_k = Q}} \frac{Q!}{r_1! r_2! \dots r_K!} \left(\prod_{k=1}^{K} s_k^{r_k}(t)\right) \left(\bigcirc_{k=1}^{K} (\mathbf{a}_{\mathbb{P}}(\theta_k))^{\circ r_k}\right), \tag{15}$$

where $\bigcirc$ denotes the sequential operation of the Hadamard product for all vectors $(\mathbf{a}_{\mathbb{P}}(\theta_k))^{\circ r_k}$.

For $Q = 2$, the possible distributions of the exponents r_k in (15) are limited to two distinct patterns. The first pattern is one exponent equals 2 and all others equal 0 (i.e., $r_k = 2$ and $r_l = 0$ for all $l \neq k$). Therefore, the form of the resulting term is $s_k^2(t)(\mathbf{a}_{\mathbb{P}}(\theta_k))^{\circ 2}$, where the number of distinct terms for this form is K (one for each source) and the number of instances (the multinomial coefficient) for each distinct term is $\frac{2!}{2!,0!,\dots,0!} = 1$. The second pattern is two distinct exponents each equals 1 and all others equal 0 (i.e., $r_k = 1$, $r_l = 1$ for $k \neq l$, and $r_m = 0$ for all $m \neq k, l$). Consequently, the term form is $s_k(t)s_l(t)\mathbf{a}_{\mathbb{P}}(\theta_k) \circ \mathbf{a}_{\mathbb{P}}(\theta_l)$. The number of distinct terms for this form is given by the combination formula $\binom{K}{2} = \frac{K(K-1)}{2}$, which counts the number of unique unordered pairs of distinct sources k, l. The multinomial coefficient for each distinct unordered pair is $\frac{2!}{1!,1!,0!,\dots,0!} = 2$. Therefore,

$$\mathbf{x}_{\mathbb{T}_3}(t) = \sum_{k=1}^{K} s_k(t)^3(\mathbf{a}_{\mathbb{P}}(\theta_k))^{\circ 3} + 3\sum_{\substack{k,l=1\\k\neq l}}^{K} s_k(t)^2 s_l(t)(\mathbf{a}_{\mathbb{P}}(\theta_k))^{\circ 2}\circ\mathbf{a}_{\mathbb{P}}(\theta_l) + 6\sum_{\substack{k,l,m=1\\k<l<m}}^{K} s_k(t)s_l(t)s_m(t)\mathbf{a}_{\mathbb{P}}(\theta_k)\circ\mathbf{a}_{\mathbb{P}}(\theta_l)\circ\mathbf{a}_{\mathbb{P}}(\theta_m). \tag{17}$$

$$\mathbf{x}_{\mathbb{T}_3}(t) = \sum_{k=1}^{K} s_k(t)^3(\mathbf{a}_{\mathbb{P}}(\theta_k))^{\circ 3} + 3\sum_{k,l=1;\ k\neq l}^{K} s_k(t)^2(\mathbf{a}_{\mathbb{P}}(\theta_k))^{\circ 2}\circ s_l(t)\mathbf{a}_{\mathbb{P}}(\theta_l) + 6\sum_{k,l,m=1;\ k<l<m}^{K} s_k(t)\mathbf{a}_{\mathbb{P}}(\theta_k)\circ s_l(t)\mathbf{a}_{\mathbb{P}}(\theta_l)\circ s_m(t)\mathbf{a}_{\mathbb{P}}(\theta_m)$$
$$+ 3(\sum_{k=1}^{K} s_k(t)^2(\mathbf{a}_{\mathbb{P}}(\theta_k))^{\circ 2}\circ\mathbf{n}_{\mathbb{P}}) + 6\sum_{1\leq k<l\leq K}[s_k(t)\mathbf{a}_{\mathbb{P}}(\theta_k)\circ s_l(t)\mathbf{a}_{\mathbb{P}}(\theta_l)]\circ\mathbf{n}_{\mathbb{P}}(t) + 3(\mathbf{A}_{\mathbb{P}}\mathbf{z}_{\mathbb{P}}\circ(\mathbf{n}_{\mathbb{P}}(t))^{\circ 2}) + (\mathbf{n}_{\mathbb{P}}(t))^{\circ 3}. \tag{20}$$

by combining these two resulting terms, the expansion of $(\mathbf{x}_{\mathbb{P}}(t))^{\circ 2}$, denoted by $\mathbf{x}_{\mathbb{T}_2}(t)$, is expressed as

$$\mathbf{x}_{\mathbb{T}_2}(t) = (\mathbf{x}_{\mathbb{P}}(t))^{\circ 2} = \mathbf{x}_{\mathbb{P}}(t)\circ\mathbf{x}_{\mathbb{P}}(t) = \tag{16}$$
$$\sum_{k=1}^{K} s_k^2(t)(\mathbf{a}_{\mathbb{P}}(\theta_k))^{\circ 2} + 2\sum_{1\leq k<l\leq K} s_k(t)s_l(t)\mathbf{a}_{\mathbb{P}}(\theta_k)\circ\mathbf{a}_{\mathbb{P}}(\theta_l).$$

When $Q = 3$, the exponents r_k in the multinomial expansion satisfy the following three distinct patterns: 1) One $r_k = 3$ and all other $r_l = 0$ for $l \neq k$; 2) One $r_k = 2$, one $r_l = 1$ (where $k \neq l$), and all other $r_m = 0$; 3) Three distinct exponents each equals 1 (i.e., $r_k = 1$, $r_l = 1$, $r_m = 1$ for $k \neq l \neq m$), and all other $r_n = 0$. Therefore, by combining the resulting terms, the expansion $\mathbf{x}_{\mathbb{T}_3}(t)$ resulting from $(\mathbf{x}_{\mathbb{P}}(t))^{\circ 3}$ is given as in (17).

Note that the expansions in (16) and (17) result in a harmonic term and cross terms, as the number of these latter grows with the higher-order expansion. In the array signal processing context, the harmonic term corresponds to the Qth-order source signal vector (i.e., $(\mathbf{s}_{\mathbb{P}}(t))^{\circ Q} = [s_1^Q(t),\ldots,s_K^Q(t)]^\top$) combined with the steering vector of the physical sensor array raised to the Hadamard power Q ($(\mathbf{a}_{\mathbb{P}}(\theta_k))^{\circ Q}$). This element-by-element power operation creates new virtual sensors located at Qp_i, where $p_i \in \mathbb{P}$. In this study, the sensor location set $\mathbb{T}_Q$, obtained as $Q\mathbb{P}$, constitutes the sensor set of the "Qth-order twin array," derived from the original sensor array, and its steering vector is expressed as

$$\mathbf{a}_{\mathbb{T}_Q}(\theta_k) = (\mathbf{a}_{\mathbb{P}}(\theta_k))^{\circ Q} = \tag{18}$$
$$[e^{j2\pi(Qp_1)(d/\lambda)sin(\theta_k)},\ldots,e^{j2\pi(Qp_N)(d/\lambda)sin(\theta_k)}]^\top.$$

□

When noise is considered ($\mathbf{n}_{\mathbb{P}}(t)$), the output vector of the second-order twin array $\mathbf{x}_{\mathbb{T}_2}(t)$ in (16) must also account for the squared noise and the signal-noise cross terms. Therefore, $\mathbf{x}_{\mathbb{T}_2}(t)$ is given as

$$\mathbf{x}_{\mathbb{T}_2}(t) = \sum_{k=1}^{K} s_k(t)^2(\mathbf{a}_{\mathbb{P}}(\theta_k))^{\circ 2} + 2\sum_{1\leq k<l\leq K} s_k(t)\mathbf{a}_{\mathbb{P}}(\theta_k) \tag{19}$$
$$\circ\, s_l(t)\mathbf{a}_{\mathbb{P}}(\theta_l) + 2\left(\mathbf{A}_{\mathbb{P}}\mathbf{s}_{\mathbb{P}}(t)\circ\mathbf{n}_{\mathbb{P}}(t)\right) + (\mathbf{n}_{\mathbb{P}}(t))^{\circ 2}.$$

For the third-order twin array, $\mathbf{x}_{\mathbb{T}_3}(t)$ in (17) is given as in (20).

B. Signal Model of the Twin Array

This subsection presents the signal model for a physical sensor array extended with its Qth-order virtual twin. It then introduces the extended array covariance matrix adopted for complex Gaussian signals (CGSs).

Let $\mathbf{x}_{\mathbb{T}_Q}(t)$, for $Q \geq 2$, represent the output vector of the Qth-order twin array, obtained by applying the Qth-order Hadamard power to the physical array output $\mathbf{x}_{\mathbb{P}}(t)$. Concatenating these two vectors forms a $2N \times T$ extended output vector, expressed as

$$\mathbf{x}_{\mathbb{E}}(t) = \begin{bmatrix}\mathbf{x}_{\mathbb{P}}^\top(t) & \mathbf{x}_{\mathbb{T}_Q}^\top(t)\end{bmatrix}^\top. \tag{21}$$

The corresponding extended array covariance matrix, estimated over T snapshots, is given by

$$\hat{\mathbf{R}}_{\mathbb{E}\mathbb{E}} = \frac{1}{T}\sum_{t=1}^{T}\mathbf{x}_{\mathbb{E}}(t)\mathbf{x}_{\mathbb{E}}^H(t). \tag{22}$$

This new $2N \times 2N$ matrix generates new difference domains through the pairwise interactions between the sensor locations of the physical array, the virtual twin array, and across the two arrays. To characterize these new domains analytically, we employ the statistically expected array covariance matrix, $\mathbf{R}_{\mathbb{E}\mathbb{E}}$. For simplicity, we assume that the output vector of the Qth-order twin array comprises only two components. Specifically, let $\mathbf{x}_{\mathbb{T}_Q}(t)$ be modeled as

$$\mathbf{x}_{\mathbb{T}_Q}(t) = \mathbf{A}_{\mathbb{T}_Q}\mathbf{s}_{\mathbb{T}_Q}(t) + \mathbf{n}_{\mathbb{T}_Q}(t), \tag{23}$$

where: $\mathbf{A}_{\mathbb{T}_Q} = [\mathbf{a}_{\mathbb{T}_Q}(\theta_1),\ldots,\mathbf{a}_{\mathbb{T}_Q}(\theta_K)] = (\mathbf{A}_{\mathbb{P}})^{\circ Q}$ is the virtual manifold matrix, $\mathbf{s}_{\mathbb{T}_Q}(t) = (\mathbf{s}_{\mathbb{P}}(t))^{\circ Q}$ is the Qth-order source signal vector, and $\mathbf{n}_{\mathbb{T}Q}(t) = (\mathbf{n}_{\mathbb{P}}(t))^{\circ Q} = [n_1^Q(t),\ldots,n_N^Q(t)]^\top$ is the Qth-order noise vector. Then, $\mathbf{R}_{\mathbb{E}\mathbb{E}}$ (with time dependence suppressed) is expressed as

$$\mathbf{R}_{\mathbb{E}\mathbb{E}} = E\left[\mathbf{x}_{\mathbb{E}}\mathbf{x}_{\mathbb{E}}^H\right] = E\left[\begin{bmatrix}\mathbf{x}_{\mathbb{P}}\\ \mathbf{x}_{\mathbb{T}_Q}\end{bmatrix}\begin{bmatrix}\mathbf{x}_{\mathbb{P}}^H & \mathbf{x}_{\mathbb{T}_Q}^H\end{bmatrix}\right] \tag{24}$$
$$= E\left[\begin{bmatrix}\mathbf{x}_{\mathbb{P}}\mathbf{x}_{\mathbb{P}}^H & \mathbf{x}_{\mathbb{P}}\mathbf{x}_{\mathbb{T}_Q}^H\\ \mathbf{x}_{\mathbb{T}_Q}\mathbf{x}_{\mathbb{P}}^H & \mathbf{x}_{\mathbb{T}_Q}\mathbf{x}_{\mathbb{T}_Q}^H\end{bmatrix}\right]$$
$$= \begin{bmatrix}E[\mathbf{x}_{\mathbb{P}}\mathbf{x}_{\mathbb{P}}^H] & E[\mathbf{x}_{\mathbb{P}}\mathbf{x}_{\mathbb{T}_Q}^H]\\ E[\mathbf{x}_{\mathbb{T}_Q}\mathbf{x}_{\mathbb{P}}^H] & E[\mathbf{x}_{\mathbb{T}_Q}\mathbf{x}_{\mathbb{T}_Q}^H]\end{bmatrix} = \begin{bmatrix}\mathbf{R}_{\mathbb{P}\mathbb{P}} & \mathbf{R}_{\mathbb{P}\mathbb{T}_Q}\\ \mathbf{R}_{\mathbb{T}_Q\mathbb{P}} & \mathbf{R}_{\mathbb{T}_Q\mathbb{T}_Q}\end{bmatrix},$$

where: $\mathbf{R}_{\mathbb{P}\mathbb{P}} = \mathbf{A}_{\mathbb{P}}E[\mathbf{s}_{\mathbb{P}}\mathbf{s}_{\mathbb{P}}^H]\mathbf{A}_{\mathbb{P}}^H + E[\mathbf{n}_{\mathbb{P}}\mathbf{n}_{\mathbb{P}}^H]$, $\mathbf{R}_{\mathbb{P}\mathbb{T}_Q} = \mathbf{A}_{\mathbb{P}}E[\mathbf{s}_{\mathbb{P}}\mathbf{s}_{\mathbb{T}_Q}^H]\mathbf{A}_{\mathbb{T}_Q}^H + E[\mathbf{n}_{\mathbb{P}}\mathbf{n}_{\mathbb{T}Q}^H]$, $\mathbf{R}_{\mathbb{T}_Q\mathbb{P}} = \mathbf{A}_{\mathbb{T}_Q}E[\mathbf{s}_{\mathbb{T}_Q}\mathbf{s}_{\mathbb{P}}^H]\mathbf{A}_{\mathbb{P}}^H + E[\mathbf{n}_{\mathbb{T}_Q}\mathbf{n}_{\mathbb{P}}^H] = \mathbf{R}_{\mathbb{P}\mathbb{T}_Q}^H$, and $\mathbf{R}_{\mathbb{T}_Q\mathbb{T}_Q} = \mathbf{A}_{\mathbb{T}_Q}E[\mathbf{s}_{\mathbb{T}_Q}\mathbf{s}_{\mathbb{T}_Q}^H]\mathbf{A}_{\mathbb{T}Q}^H + E[\mathbf{n}_{\mathbb{T}_Q}\mathbf{n}_{\mathbb{T}_Q}^H]$. As such, $\mathbf{R}_{\mathbb{E}\mathbb{E}}$ in (24) can be expressed - in a similar way to the way of expressing $\mathbf{R}_{\mathbb{P}\mathbb{P}}$ in (4) w.r.t. (3) - as

$$\mathbf{R}_{\mathbb{E}\mathbb{E}} = \tag{25}$$
$$\begin{bmatrix}\sum_{k=1}^{K}\sigma_k^2\mathbf{D}_{\mathbb{P}}(\theta_k) + \sigma_n^2\mathbf{I}_N & \sum_{k=1}^{K}\varsigma_k^*\mathbf{D}_{\mathbb{P}\mathbb{T}_Q}(\theta_k) + \eta_n^*\mathbf{I}_N\\ \sum_{k=1}^{K}\varsigma_k\mathbf{D}_{\mathbb{T}_Q\mathbb{P}}(\theta_k) + \eta_n\mathbf{I}_N & \sum_{k=1}^{K}\sigma_k^{2Q}\mathbf{D}_{\mathbb{T}_Q}(\theta_k) + \sigma_n^{2Q}\mathbf{I}_N\end{bmatrix},$$

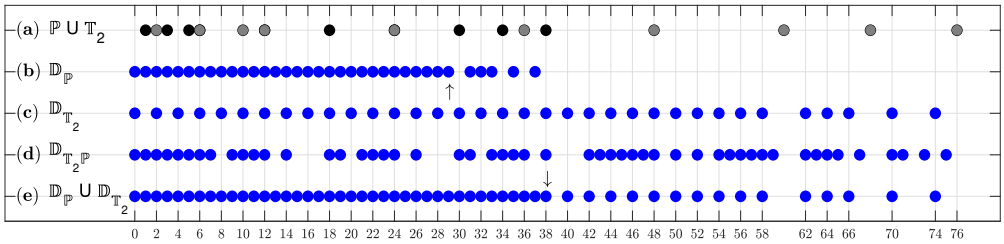

Fig. 1. Sensor locations of a 10-sensor second-order dilated nested array ($\mathbb{P}$), its second-order twin ($\mathbb{T}_2$), their respective difference arrays ($\mathbb{D}_{\mathbb{P}}$, $\mathbb{D}_{\mathbb{T}_2}$), and their difference co-array ($\mathbb{D}_{\mathbb{T}_2\mathbb{P}}$), where black, gray, and blue bullets represent the physical sensors, the twin array virtual sensors, and the virtual difference sensors, respectively. $\mathbb{P} = \{1, 3, 5, 6, 12, 18, 24, 30, 34, 38\}$ and $\mathbb{T}_2 = 2\mathbb{P}$.

where $\sigma_k^2 = E[s_k(t)s_k^*(t)]$, $\sigma_k^{2Q} = E[s_k^Q(t)(s_k^Q(t))^*]$, $\varsigma_k = E[s_k^Q(t)s_k^*(t)]$, and $\eta_n = E[n_i^Q(t)n_i^H(t)]$.

For a CGS $s_k(t)$ with zero mean and variance σ_k^2, the expectation of the signal with its conjugate ($E[s_k(t)s_k^*(t)]$) is the expectation of the squared magnitude of the signal ($E[|s_k(t)|^2]$), which in turn is the signal variance/power σ_k^2. When $Q > 1$, the expectation $E[s_k^Q(t)(s_k^Q(t))^*]$ equals $E[|s_k(t)|^{2Q}]$, which is the statistical $2Q$th moment of the signal. For a Gaussian distribution, this higher-order statistic [1] is given by

$$E[|s_k(t)|^{2Q}] = Q!\,(E[|s_k(t)|^2])^Q = Q!\,\sigma_k^{2Q}. \tag{26}$$

Since the $2Q$th-order moment for any CGS with zero mean and variance σ^2 follows (26), it also holds that $E[|n_i(t)|^{2Q}] = Q!\,\sigma_n^{2Q}$. However, the element $[\mathbf{x}_{\mathbb{T}_Q}(t)]_i$ also contains cross terms. These involve multiple signals and signal-noise interactions. The expectations of these terms are also $2Q$th-order statistics. This is because raising the weighted sum to the power Q, ($[(\mathbf{x}_{\mathbb{P}}(t))^{\circ Q}]_i$), distributes the exponent evenly across each term of the expansion.

Explicitly, assume a cross-signal term of L independent CGSs, each with zero mean and variance σ_l^2, is defined as $x_s(t) = s_1^{r_1}(t)s_2^{r_2}(t)\dots s_L^{r_L}(t)$, where $r_l \geq 0$ and $\sum_{l=1}^L r_l = Q$. Then, $E\left[x_s(t)x_s^*(t)\right]$ is

$$\begin{aligned} E\left[x_s(t)x_s^*(t)\right] &= E\left[(s_1^{r_1}(t)\dots s_L^{r_L}(t))(s_1^{r_1}(t)\dots s_L^{r_L}(t))^*\right] \\ &= E\left[|s_1(t)|^{2r_1}\dots|s_L(t)|^{2r_L}\right] \\ &= E\left[|s_1(t)|^{2r_1}\right]\dots E\left[|s_L(t)|^{2r_L}\right]. \end{aligned} \tag{27}$$

According to (26), $E\left[|s_l(t)|^{2r_l}\right] = r_l!\,\sigma_l^{2r_l}$. Therefore, the total expected value becomes

$$E\left[x_s(t)x_s^*(t)\right] = \prod_{l=1}^{L}\left(r_l!\;\sigma_l^{2r_l}\right). \tag{28}$$

When $\sigma_l^2 = \sigma^2$ for all l, the generalization in (28) simplifies as $\prod_{l=1}^L \sigma_l^{2r_l} = \sigma^{2(r_1+r_2+\dots+r_L)} = \sigma^{2Q}$. Thus, the formula becomes

$$E\left[x_s(t)x_s^*(t)\right] = (\prod_{l=1}^{L} r_l!)\,\sigma^{2Q}. \tag{29}$$

For the signal-noise cross term $x_{sn}(t)$ defined as $x_{sn}(t) = (s_1^{r_1}(t)\dots s_L^{r_L}(t))(n_1^{r_1}(t)\dots n_M^{r_M}(t))$, where $\sum_{l=1}^L r_l + \sum_{m=1}^M r_m = Q_s + Q_n = Q$, $E\left[x_{sn}(t)x_{sn}^*(t)\right]$ is $(\prod_{l=1}^L E[|s_l(t)|^{2r_L}])(\prod_{m=1}^M E[|n_m(t)|^{2r_m}])$. Therefore, the expectation becomes

$$E\left[x_{sn}(t)x_{sn}^*(t)\right] = (\prod_{l=1}^{L} r_l!)\,(\prod_{m=1}^{M} r_m!)\,(\sigma_l^2)^{Q_s}\,(\sigma_n^2)^{Q_n}, \tag{30}$$

where $Q_s = \sum_{l=1}^L r_l$, $Q_n = \sum_{m=1}^M r_m$, and $Q_s + Q_n = Q$. In $[(\mathbf{x}_{\mathbb{P}}(t))^{\circ Q}]_i$, $x_{sn}(t)$ is of the form $s_1^{r_1}(t)\dots s_L^{r_L}(t)\;n_i^{Q_n}(t)$, where $\sum_{l=1}^L r_l + Q_n = Q_s + Q_n = Q$. Therefore, this special case is given as

$$E\left[x_{sn}(t)x_{sn}^*(t)\right] = (\prod_{l=1}^{L} r_l!)(Q_n!)(\sigma_s^2)^{Q_s}\,(\sigma_n^2)^{Q_n}, \tag{31}$$

where $Q_s = \sum_{l=1}^L r_l$, and $Q_s + Q_n = Q$.

However, note that when $Q > 1$, for a circularly symmetric CGS, the expectation of the form $E[s_k^Q(t)(s_k(t))^*]$ is zero. This means the covariance matrix $\mathbf{R}_{\mathbb{T}_Q\mathbb{P}}$, which includes the steering matrix $\mathbf{D}_{\mathbb{T}_Q\mathbb{P}}$, is zero. Fig. 1 shows the sensor locations for a 10-element dilated nested array (DNA) of order $Q_f + 1$, as defined in [16], and its second-order twin array. The figure also presents the difference arrays for each and their difference co-array. Since the covariance matrix is zero, the DOF within the difference co-array $\mathbb{D}_{\mathbb{T}_2\mathbb{P}}$ is non-functional.

Therefore, in this study, which is on circularly symmetric CGSs, the extended covariance matrix $\mathbf{R}_{\mathbb{E}\mathbb{E}}$ is formed and defined as a block column matrix, given by

$$\mathbf{R}_{\mathbb{E}\mathbb{E}} = \begin{bmatrix} \mathbf{R}_{\mathbb{P}\mathbb{P}} \\ \mathbf{R}_{\mathbb{T}_Q\mathbb{T}_Q} \end{bmatrix}, \tag{32}$$

where $\mathbf{R}_{\mathbb{P}\mathbb{P}} = E[\mathbf{x}_{\mathbb{P}}(t)\mathbf{x}_{\mathbb{P}}^H(t)]$ and $\mathbf{R}_{\mathbb{T}_Q\mathbb{T}_Q} = E[\mathbf{x}_{\mathbb{T}_Q}(t)\mathbf{x}_{\mathbb{T}_Q}^H(t)]$. Their sample estimates are given by $\hat{\mathbf{R}}_{\mathbb{P}\mathbb{P}} = \frac{1}{T}\sum_{t=1}^T \mathbf{x}_{\mathbb{P}}(t)\mathbf{x}_{\mathbb{P}}^H(t)$ and $\hat{\mathbf{R}}_{\mathbb{T}_Q\mathbb{T}_Q} = \frac{1}{T}\sum_{t=1}^T \mathbf{x}_{\mathbb{T}_Q}(t)\mathbf{x}_{\mathbb{T}_Q}^H(t)$, respectively.

In array signal processing with CGSs, as seen in (4), the variance (the second-order moment) of the CGS dominates the structure of the array covariance matrix $\mathbf{R}_{\mathbb{P}\mathbb{P}}$. This dominance is also revealed by the eigenvalue decomposition (EVD) of $\hat{\mathbf{R}}_{\mathbb{P}\mathbb{P}}$, particularly when the impinging signals are of equal power, where the average of the largest eigenvalues (G_{P_L}) corresponds to the signal power ($G_{P_L} \approx \sigma_k^2 + \sigma_n^2$), while the average of the smallest eigenvalues corresponds to the noise variance ($G_{P_S} \approx \sigma_n^2$). This creates a distinct eigenvalue gap, which is essential for the performance of subspace-based DOA estimation algorithms.

In our approach, which uses the matrix $\mathbf{R}_{\mathbb{T}_Q\mathbb{T}_Q}$, the $2Q$th-order moments of the source signal — generated by the Qth-order twin array — can dominate $\mathbf{R}_{\mathbb{E}\mathbb{E}}$. This dominance occurs specifically when the received signal power is high (e.g., $\sigma^2 \geq 1$ Watt), so that $Q!\,\sigma^{2Q} \gg \sigma^2$. For example, the $2Q$th-order moment is $Q!\,\sigma^{2Q}$: for a second-order twin array ($Q = 2$), this is the fourth moment ($\approx 2\sigma^4$); for $Q = 3$, the sixth moment ($\approx 6\sigma^6$); and for $Q = 4$, the eighth moment ($\approx 24\sigma^8$). Thus, the $2Q$th-order moment increases exponentially with Q and inevitably becomes the dominant component under such a condition (under high received signal power condition).

Nevertheless, in practical applications where signals are received with low power ($\sigma^2 \ll 1$ Watt), the $2Q$th-order moments become negligible. This is because the inequality $Q!\,\sigma^{2Q} \ll \sigma^2$ also holds. As a result, the contribution from the physical sensor array and its Gaussian properties dominates the structure of the extended covariance matrix. Crucially, however, the extension still provides the benefit of exploiting the difference domain of the Qth-order twin array, as demonstrated in Section V. It is important to note that the purpose of this study is to introduce and validate the Qth-order twin array concept by obtaining valid spatial spectra using standard second-order DOA estimation algorithms. Future array designs can therefore be specifically optimized to maximize the combined DOF offered by $\mathbb{P} \cup \mathbb{T}_Q$.

IV. DISCUSSION

This section discusses and compares the DOA estimation performance of a physical array operating alone with that of its combination with a virtual twin array. The comparison aims to investigate the impact of incorporating the Qth-order twin array on the structure and properties of the extended array covariance matrix.

This section uses the improved co-prime nested array (ICNA) geometry because, for certain values of N, the physical array ($\mathbb{P}$) provides the same number of uniform DOF as the combined array ($\mathbb{P} \cup \mathbb{T}_Q$). For instance, an ICNA with $N = 7$ physical sensors yields 16 uniform DOF. When combined with its second-order virtual twin array ($\mathbb{T}_2$) — whose sensor locations are given by $2\mathbb{P} = [2, 4, 6, 8, 10, 12, 14]$ — the number of uniform DOF remains 16.

In this and the following section, unless stated otherwise, the source signals are modeled as uncorrelated, complex Gaussian random processes with equal power. The signals are assumed to arrive from directions that are uniformly distributed in angle. The sensor noise is modeled as a complex, zero-mean Gaussian process that is spatially and temporally white and uncorrelated with the source signals. The array covariance matrix is estimated from 5,000 temporal snapshots. The spatial spectra are visualized using the subspace-based MUSIC algorithm [43], [45]. The accuracy of the DOA estimation is quantified by the root mean square error (RMSE). RMSE is calculated from estimates provided by the high-resolution root-MUSIC algorithm [44]. It is defined as $\text{RMSE} = \sqrt{\frac{1}{KY}\sum_{y=1}^{Y}\sum_{k=1}^{K}(\hat{\bar{\theta}}_k^{(y)} - \bar{\theta}_k)^2}$, where $\hat{\bar{\theta}}_k^{(y)}$ is the estimated direction of the kth source in the yth Monte Carlo trial ($Y = 500$ trials), and $\bar{\theta}_k$ is the corresponding true direction. The true direction is expressed in spatial frequency units as $(d/\lambda)\sin(\theta_k)$.

When applied to the covariance matrix of the physical array $\hat{\mathbf{R}}_{\mathbb{P}\mathbb{P}}$, the MUSIC algorithm achieves excellent DOA estimation for 12 signals (Fig. 2(a)). This is due to the clear gap between the signal and noise eigenvalues, as revealed by the eigenvalue decomposition plot accompanying Fig. 2(a). In contrast, the performance of the MUSIC algorithm deteriorates for the same signals when applied to the extended covariance matrix $\hat{\mathbf{R}}_{\mathbb{E}\mathbb{E}}$, which is formed by combining the physical sensor array with its virtual twin (where $\mathbf{x}_{\mathbb{E}}(t) = [\mathbf{x}_{\mathbb{P}}^{\top}(t)\ \mathbf{x}_{\mathbb{T}_2}^{\top}(t)]^{\top}$), as shown in Fig. 2(b).

The incorporation of the virtual twin array distorts the structure of the extended covariance matrix. Specifically, the EVD plot in Fig. 2(c) shows that the average eigenvalue of $\hat{\mathbf{R}}_{\mathbb{P}\mathbb{P}}$ (G_P) is about $\sigma_k^2+\sigma_n^2$, while that of $\hat{\mathbf{R}}_{\mathbb{T}_2\mathbb{T}_2}$ (G_{T_2}) is about $2\sigma_k^4 + 2\sigma_n^4$. This shows that the higher-order moment inflates the eigenvalue spectrum. Contributions from cross-signal and signal-noise interactions further amplify this effect, as seen in the degraded spatial spectrum of Fig. 2(b). The Toeplitz-averaged matrix $\hat{\mathbf{R}}_{\mathbb{U}}$ reduces this amplification (as shown in G_{U_L} and G_{U_S}) due to its correlation vector $\mathbf{r}_{\mathbb{U}}$. According to (7), this vector averages the correlation statistics for each different difference. However, it cannot prevent the Qth-order twin array terms from dominating the covariance matrix. This issue is also seen in Figs. 5(a), 7(a), and 8(a), where the Qth-order twin array inflates the eigenvalue spectrum, shrinking the gap between large and small eigenvalues and impairing the algorithm ability to exploit subspace orthogonality.

Therefore, it is necessary to reduce this numerical amplification and its adverse effect on the extended covariance matrix. This can be achieved by scaling, or "sinking," the twin array output vector. The principle is to scale the signal amplitudes down. This suppresses the higher-order moment ($Q!\,\sigma^{2Q}$) relative to the second-order moment (σ^2). By scaling $\mathbf{x}_{\mathbb{T}_2}(t)$ by $1/\sqrt{10}$, as shown in Fig. 2(d), we see a significant improvement in DOA estimation performance for the 12 signals compared to the non-scaled case in Fig. 2(b).

This improvement continues with greater attenuation. For instance, when a divisor of $\sqrt{100}$ replaces $\sqrt{10}$, estimation accuracy improves, as shown in Fig. 2(e). Beyond this point, however, the accuracy plateaus. Increasing the divisor further to $\sqrt{10^3}$ or $\sqrt{10^6}$ (see Figs. 2(f) and 2(g)) produces no additional improvement. The figures also show that the averages of the large and small eigenvalues (G_{U_L} and G_{U_S}) remain unchanged. This is because the extended array covariance matrix now becomes dominated by the original physical array, rather than its virtual twin, as indicated by $G_{T_2} \ll G_P$ in the figures.

Nevertheless, applying attenuation to prevent the twin array from numerically dominating the covariance matrix structure is not always necessary. This is particularly true when the received signal power is low (e.g., σ^2 is below 1 Watt, which corresponds to typical practical levels such as -70 dBm). Under such low-power conditions, the Hadamard product operation in the twin array output further attenuates the signal amplitude. As a result, the contribution from the original physical array

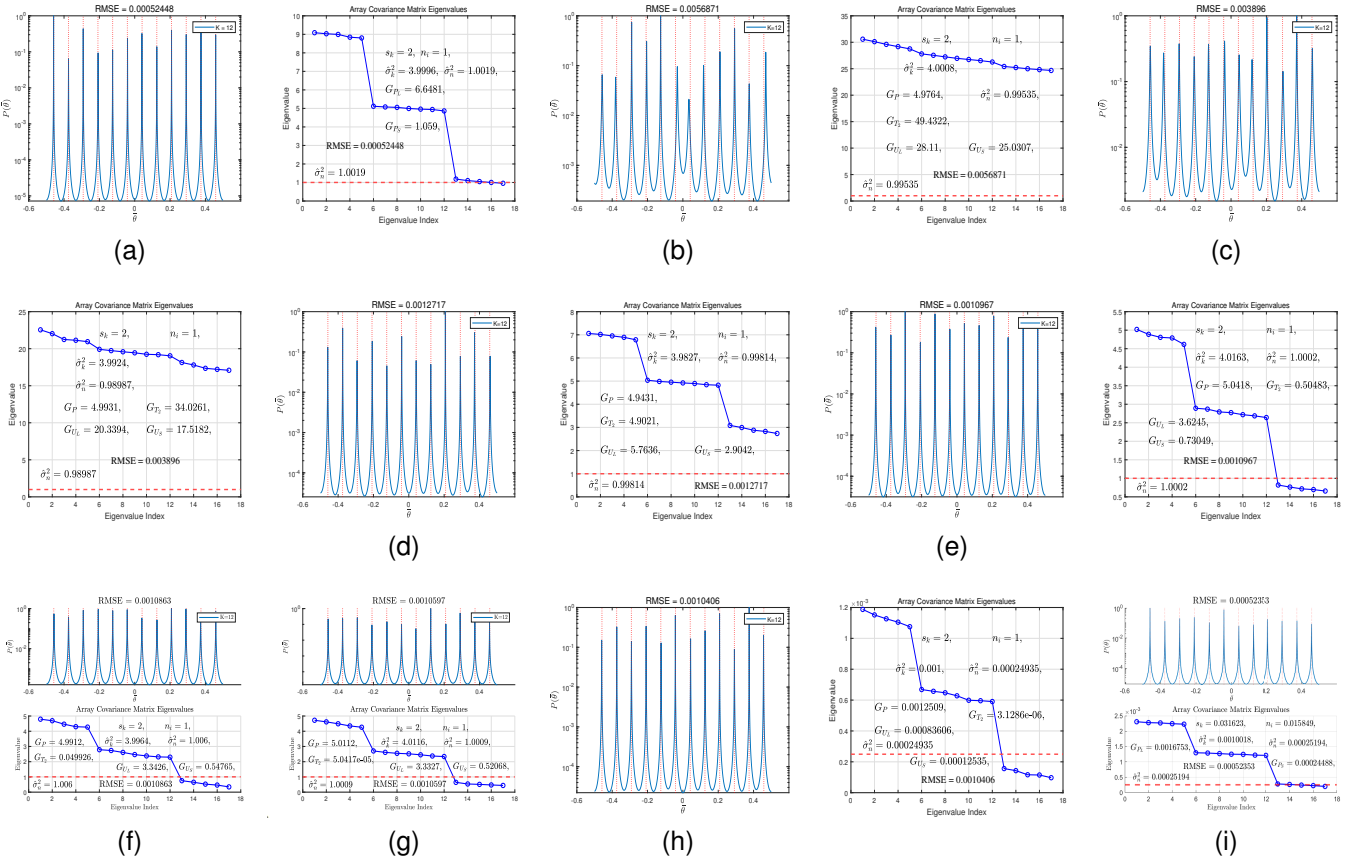

Fig. 2. MUSIC spectra $P(\bar{\theta})$ and eigenvalue decomposition (EVD) of the covariance matrices $\hat{\mathbf{R}}_{\mathbb{PP}}$ for an improved co-prime nested array (ICNA) geometry and $\hat{\mathbf{R}}_{\mathbb{EE}}$ for the ICNA combined with the second-order twin array, whose output vector $\mathbf{x}_{\mathbb{T}_2}(t)$ is generated as $(\mathbf{x}_{\mathbb{P}}(t))^{\circ 2}$. The scenario involves $K = 12$ complex Gaussian signals (CGSs) with angles $\bar{\theta}_k = -0.458 + 0.916(k-1)/(K-1)$ for $1 \le k \le K$, $N = 7$ sensors, and $T = 5 \times 10^3$ snapshots. Unless otherwise specified, the source power is $\sigma_k^2 = 36$ dBm and the noise power is $\sigma_n^2 = 30$ dBm (SNR = 6 dB). **(a)** Spectrum using only the physical array output $\mathbf{x}_{\mathbb{P}}(t)$. **(b)** Spectrum using the extended output vector $\mathbf{x}_{\mathbb{E}}(t)$. **(c)** Spectrum using $\mathbf{x}_{\mathbb{E}}(t)$ with $\mathbf{x}_{\mathbb{T}_2}(t)$ made only of the harmonic-signal and -noise spaces. **(d-g)** Spectrum using a scaled output vector within $\mathbf{x}_{\mathbb{E}}(t)$: $\mathbf{x}_{\mathbb{T}_2}(t)/\sqrt{f}$ with scaling factor $f = 10, 10^2, 10^3, 10^6$. **(h)** $\mathbf{x}_{\mathbb{E}}(t)$ with low-power sources: $\sigma_k^2 = -30$ dBm, $\sigma_n^2 = -36$ dBm. **(i)** $\mathbf{x}_{\mathbb{P}}(t)$ with $\sigma_k^2 = -30$ dBm, $\sigma_n^2 = -36$ dBm.

naturally dominates the extended covariance matrix structure. Fig. 2(h) illustrates this scenario for a received power of -30 dBm and a noise floor of -36 dBm. Here, a clear gap is observed between the small and large eigenvalues. This eigenvalue structure indicates that the matrix retains statistical properties consistent with a Gaussian model. In conjunction with Fig. 2(i), these results show that second-order statistics predominate, and the higher-order moments in this case are too weak to contaminate the matrix structure.

However, when the signal level is low and further reduced by the twin array, amplitude attenuation can drive small eigenvalues (those unlinked to high-power directions) to negative values, rendering the covariance matrix indefinite. For example, with 15 signals arriving from directions $\bar{\theta}_k = -0.435 + 0.87(k-1)/(K-1)$ for $1 \le k \le K$, some small eigenvalues become negative, as shown in Fig. 3(a). The effect intensifies and these eigenvalues drift farther from zero when the directions are $\bar{\theta}_k = -0.465 + 0.93(k-1)/(K-1)$ (Fig. 3(b)). Importantly, this bias in noise power does not destroy eigenspace orthogonality. Since $\mathbf{R}_{\mathbb{EE}}$ is still Hermitian, the signal and noise subspaces remain orthogonal, even with negative eigenvalues, and the required eigenvalue gap for their separation also remains well defined.

In other words, this indefiniteness has no effect on subspace-based DOA estimation algorithms. In Figs. 3(a) and 3(b), the MUSIC algorithm, applied directly to indefinite matrices, yields spatial spectra that align with the true directions. Similar alignment appears in Figs. 3(c) and 3(d), where the MATLAB `pmusic` function is used on the same matrices. Thus, these indefinite covariance matrices, like the indefinite Toeplitz covariance matrix in [43], do not affect subspace-based DOA estimation. Nevertheless, zeroing, thresholding, or regularizing $\hat{\mathbf{R}}_{\mathbb{U}}$, as in Fig. 3(e), restores the positive semi-definite property, as shown in Fig. 3(f).

V. Simulation Results

This section presents simulation results to validate four key aspects and is therefore organized into four subsections. The first subsection shows the enhancement in uniform DOF achieved by combining the physical array with its virtual twin. This combination increases the number of detectable sources beyond the limit imposed by the difference array of the physical array alone. The second subsection extends this validation to higher-order twin arrays (specifically, third-

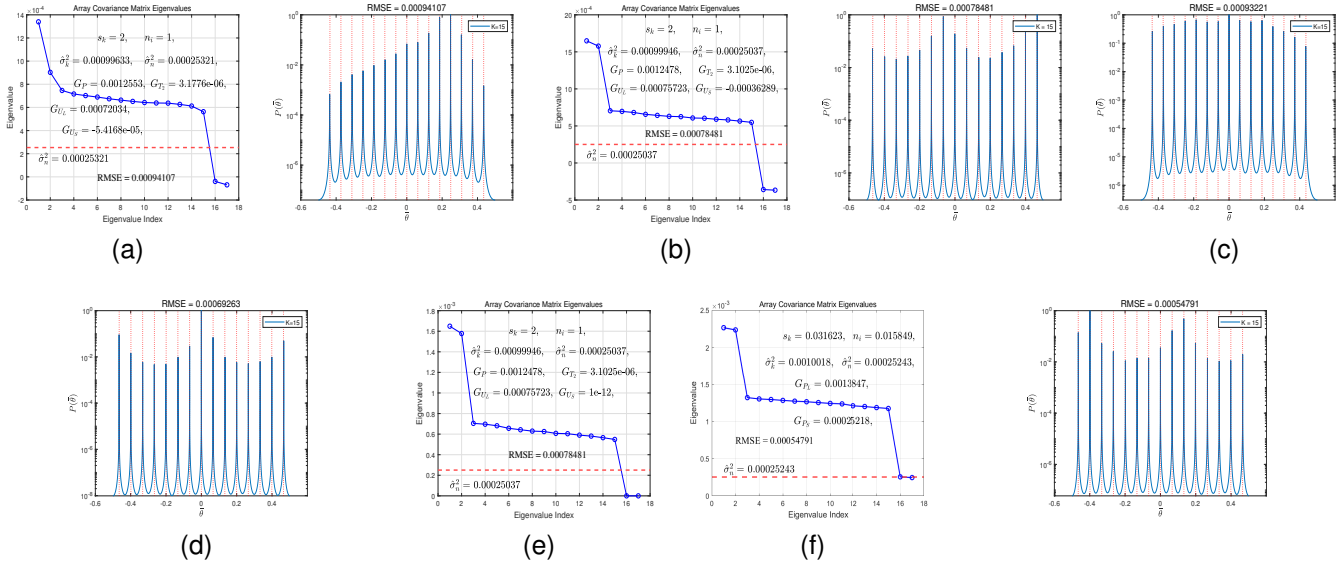

Fig. 3. $P(\bar{\theta})$ and EVD of $\hat{\mathbf{R}}_{\mathbb{EE}}$ for the 7-sensor ICNA combined with its second-order twin array. In this simulation scenario, $K = 15$ CGSs, $T = 5 \times 10^3$, $\sigma_k^2 = -30$ dBm, and $\sigma_n^2 = -36$ dBm (SNR = 6 dB). Source angles are defined for $1 \le k \le K$ as: **(a)** $\bar{\theta}_k = -0.435 + 0.87(k-1)/(K-1)$. **(b)** $\bar{\theta}_k = -0.465 + 0.93(k-1)/(K-1)$. **(c)** $\bar{\theta}_k = -0.435 + 0.87(k-1)/(K-1)$, **(d)** $\bar{\theta}_k = -0.465 + 0.93(k-1)/(K-1)$. **(e)** $\bar{\theta}_k = -0.465 + 0.93(k-1)/(K-1)$ with thresholding (G_{U_S}). **(f)** EVD of $\hat{\mathbf{R}}_{\mathbb{PP}}$ and the associated $P(\bar{\theta})$ with $\bar{\theta}_k = -0.465 + 0.93(k-1)/(K-1)$.

and fourth-order) to demonstrate their ability to handle more sources. These numbers correspond to their theoretically enhanced DOF. The third subsection compares estimation accuracy across different combined configurations to quantify the benefits of higher-order twin arrays. Finally, the fourth subsection examines the performance of these virtual arrays under more realistic conditions, involving random distributions of source powers and angles of arrival.

A. Validation with Second-Order Twin Arrays

This subsection presents simulation results to quantify the aggregate DOF obtained by integrating a physical sensor array with its corresponding twin array. The employed configuration is a Qth-order dilated nested array (DNA), as specified in [16]. With $N = 11$ sensors, the sensor positions for the second-order DNA are provided by the set $\mathbb{P} = \{1, 3, 5, 6, 12, 18, 24, 30, 36, 40, 44\}$. The associated second-order twin array is defined as $\mathbb{T}_2 = \{2, 6, 10, 12, 24, 36, 48, 60, 72, 80, 88\}$.

The second-order DNA structure alone achieves 35 uniform DOF in its difference array, $\mathbb{D}_{\mathbb{P}}$. When combined with its twin array, the resulting structure provides a total of 44 uniform DOFs, collected from the union $\mathbb{D}_{\mathbb{P}} \cup \mathbb{D}_{\mathbb{T}_2}$.

Fig. 4 depicts the spatial spectra for 40 and 44 CGSs. The results show sharply defined peaks that accurately correspond to the true directions of arrival, validating the capability to resolve a number of sources exceeding the 35-source limit possible with the second-order DNA operating alone.

B. Validation with High-Order Twin Arrays

This subsection extends the validation to third- and fourth-order twin arrays. We present spatial spectra that use the enhanced uniform DOF. We also provide an eigenvalue analysis

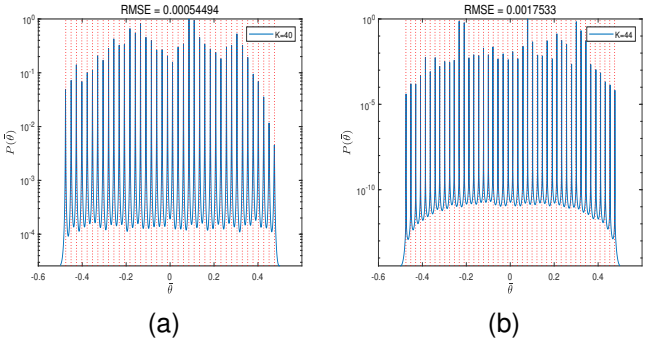

Fig. 4. MUSIC spectra computed from $\hat{\mathbf{R}}_{\mathbb{EE}}$ for a second-order DNA with its second-order twin array. **(a)** $K = 40$ CGSs. **(b)** $K = 44$ CGSs.. Common parameters: $N = 11$, $T = 5000$, $\sigma_k^2 = -30$ dBm, $\sigma_n^2 = -36$ dBm, $\bar{\theta}_k = -0.475 + 0.95(k-1)/(K-1)$, $1 \le k \le K$.

of the extended covariance matrix to observe the effects of higher-order statistical moments.

We continue using the 11-sensor second-order DNA configuration from the previous subsection. The combined array $\mathbb{P} \cup \mathbb{T}_3$, where the third-order virtual array is given by $\mathbb{T}_3 = \{3, 9, 15, 18, 36, 54, 72, 90, 108, 120, 132\}$, provides 39 uniform DOF. Similarly, the combined array $\mathbb{P} \cup \mathbb{T}_4$, where the fourth-order virtual array is defined by $\mathbb{T}_4 = 4\mathbb{P}$, provides 41 uniform DOF.

Fig. 5(a) and its eigenvalue plot show results for 38 CGSs using the combined array $\mathbb{P} \cup \mathbb{T}_3$. The higher-order statistics from the twin array ($G_{T_3} \propto 6\sigma_k^6$) degrade performance by causing missing and misaligned spectral peaks due to the numerical amplification. However, as illustrated in Fig. 5(b) and Fig. 6(a), scaling and calibration counteract this amplification, thereby improving performance. In contrast,

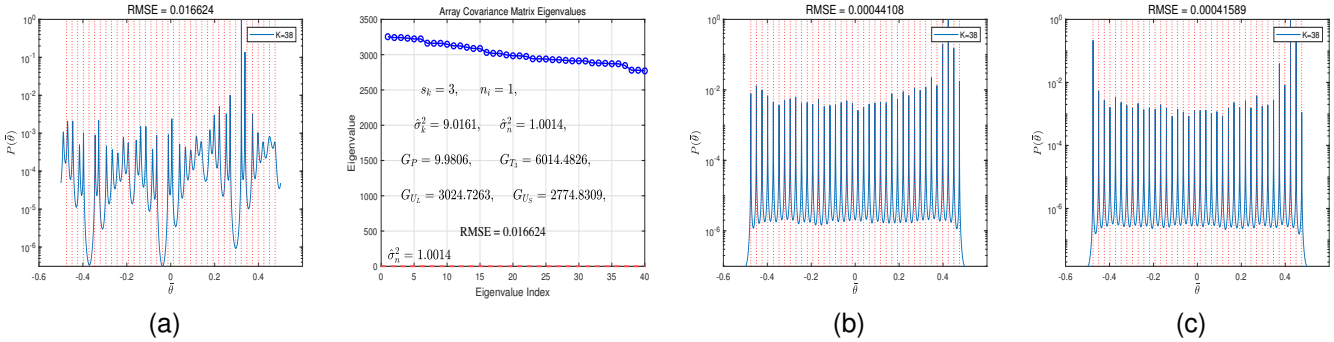

Fig. 5. $P(\bar{\theta})$ and EVD of $\hat{\mathbf{R}}_{\mathbb{EE}}$ for an eleven-sensor second-order DNA with the third-order twin array, whose output vector $\mathbf{x}_{\mathbb{T}_3}(t)$ is generated as $(\mathbf{x}_{\mathbb{P}}(t))^{\circ 3}$. The scenario involves $K = 38$ sources with arrival angles defined by $\bar{\theta}_k = -0.475 + 0.95(k-1)/(K-1)$ for $1 \le k \le K$, using $T = 5000$ snapshots. **(a)** $\mathbf{x}_{\mathbb{T}_3}(t)$ with $\sigma_k^2 = 39.5$ dBm and $\sigma_n^2 = 30$ dBm. **(b)** $\mathbf{x}_{\mathbb{T}_3}(t)/\sqrt{10^3}$ with $\sigma_k^2 = 39.5$ dBm and $\sigma_n^2 = 30$ dBm. **(c)** $\mathbf{x}_{\mathbb{T}_3}(t)$ with $\sigma_k^2 = -30$ dBm and $\sigma_n^2 = -39.5$ dBm.

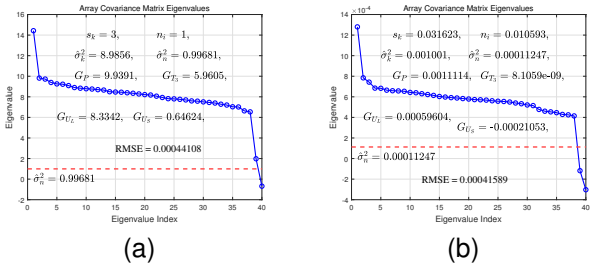

Fig. 6. EVD of $\hat{\mathbf{R}}_{\mathbb{EE}}$ for an eleven-sensor second-order DNA with its third-order twin array. This scenario involves $K = 38$ sources with angles defined by $\bar{\theta}_k = -0.475+0.95(k-1)/(K-1)$ for $k = 1, \ldots, K$, using $T = 5000$ snapshots. **(a)** $\mathbf{x}_{\mathbb{T}_3}(t)/\sqrt{10^3}$ with $\sigma_k^2 = 39.5$ dBm and $\sigma_n^2 = 30$ dBm. **(b)** $\mathbf{x}_{\mathbb{T}_3}(t)$ with $\sigma_k^2 = -30$ dBm and $\sigma_n^2 = -39.5$ dBm.

Fig. 6(b) shows that under low signal power, the third-order twin array attenuates rather than amplifies signal amplitudes, which allows the original array to dominate in the extended covariance matrix while still benefiting from the enhanced DOF. Therefore, as shown in Fig. 5(c), the combined array detects more sources than the original sensor array.

Figs. 7(a) and 8(a) present the results for the array combined with its fourth-order twin for 38 CGSs. These results show that the colossal higher-order moment ($G_L \propto 24\sigma_k^8$) severely distorts the covariance matrix structure. Scaling addresses this distortion, resulting in accurate DOA estimation for all 38 signals (Figs. 7(b) and 8(b)), while direct accurate estimation occurs when the incoming signal amplitude is below 1 V (Fig. 7(c)).

C. Accuracy Comparison: Standard vs. Higher-Order Twin Arrays

This subsection evaluates the accuracy of DOA estimation by comparing the performance of a physical sensor array paired with its standard (second-order) twin array against its pairings with higher-order (third- and fourth-order) virtual twins.

We utilize the ICNA as the physical sensor array. For a configuration with $N = 13$ sensors, the combined arrays $\mathbb{P} \cup \mathbb{T}_2$, $\mathbb{P} \cup \mathbb{T}_3$, and $\mathbb{P} \cup \mathbb{T}_4$ each yield 52 uniform DOF. Similarly, for $N = 15$ sensors, these combinations provide 70 uniform DOF.

Table I lists the RMSE values for scenarios involving 35 and 50 sources, across various maximum angular separations. The results indicate that the configurations incorporating higher-order twin arrays achieve superior estimation accuracy compared to the standard second-order configuration. This trend is consistently demonstrated in Table II, which shows that the fourth-order configuration yields the lowest RMSE.

The improvement in accuracy, despite equal numbers of uniform DOF, is due to the way the higher-order twin arrays are constructed. Although the output vector of a higher-order twin array contains more cross-term interactions, the inherent amplitude attenuation associated with the higher-order expansion mitigates the numerical presence of these terms in the extended covariance matrix. This may result in a cleaner statistical representation, which, in turn, may lead to more stable and accurate DOA estimates.

D. Performance Under Non-Ideal Conditions

This subsection evaluates the performance of the twin array under realistic, non-ideal conditions, including signals with non-zero means and random distributions for both power levels and angles of arrival.

Fig. 9(a) displays the spatial spectrum for the physical-virtual array structure when the received CGSs contain non-zero mean components. Although CGSs in typical communication systems usually have a zero mean or a mean power significantly below the noise floor, this simulation assumes that the mean power of each signal equals the noise power ($|\mu_k|^2 = 0.00025$ mWatt). As shown, this non-zero mean degrades the DOA estimation performance compared to the zero-mean baseline in Fig. 7(c). However, applying mean removal prior to the extended covariance estimation (by computing $\mathbf{x}_{\mathbb{P}} - E[\mathbf{x}_{\mathbb{P}}]$) leads to improved estimation performance, as depicted in Fig. 9(b).

Fig. 10(a) depicts the spatial spectrum for a scenario where the time-varying power levels of the CGSs follow a Log-Normal distribution. The received power has a mean of -30 dBm and a standard deviation of 3 dB, truncated to ± 2

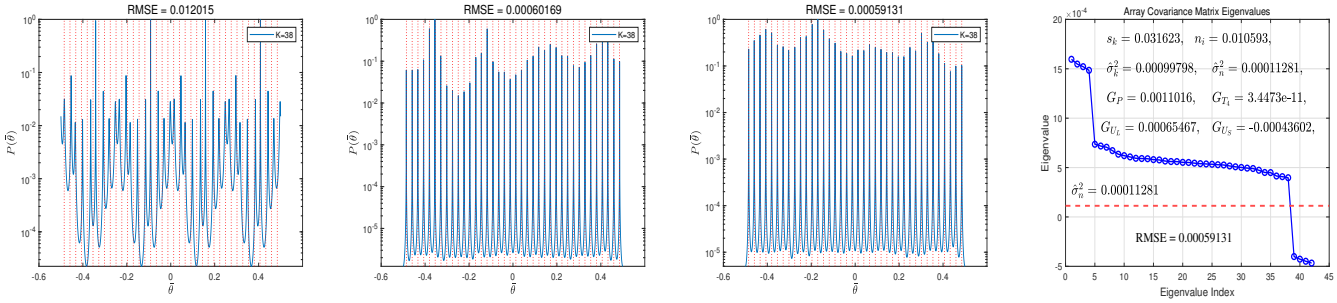

Fig. 7. $P(\bar{\theta})$ and EVD of $\hat{\mathbf{R}}_{\mathbb{EE}}$ for an eleven-sensor second-order DNA with the fourth-order twin array, whose output vector $\mathbf{x}_{\mathbb{T}_4}(t)$ is generated as $(\mathbf{x}_{\mathbb{P}}(t))^{\circ 4}$. The scenario involves $K = 38$ sources with arrival angles defined by $\bar{\theta}_k = -0.485 + 0.97(k-1)/(K-1)$ for $1 \le k \le K$, using $T = 5000$ snapshots. (a) $\mathbf{x}_{\mathbb{T}_4}(t)$ with $\sigma_k^2 = 39.5$ dBm and $\sigma_n^2 = 30$ dBm. (b) $\mathbf{x}_{\mathbb{T}_4}(t)/\sqrt{3 \times 10^4}$ with $\sigma_k^2 = 39.5$ dBm and $\sigma_n^2 = 30$ dBm. (c) $\mathbf{x}_{\mathbb{T}_4}(t)$ with $\sigma_k^2 = -30$ dBm and $\sigma_n^2 = -39.5$ dBm.

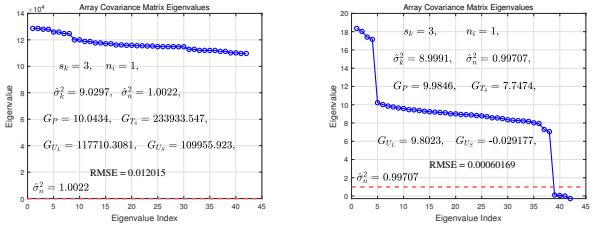

Fig. 8. EVD of $\hat{\mathbf{R}}_{\mathbb{EE}}$ for an eleven-sensor second-order DNA with its fourth-order twin. This scenario involves K = 38 sources with angles defined by $\bar{\theta}_k = -0.485 + 0.97(k-1)/(K-1)$ for $k = 1, \ldots, K$, using $T = 5000$ snapshots. **(a)** $\mathbf{x}_{\mathbb{T}_4}(t)$ with $\sigma_k^2 = 39.5$ dBm and $\sigma_n^2 = 30$ dBm. **(b)** $\mathbf{x}_{\mathbb{T}_4}(t)/\sqrt{3 \times 10^4}$ with $\sigma_k^2 = 39.5$ dBm and $\sigma_n^2 = 30$ dBm.

standard deviations (-36 dBm to -24 dBm) to prevent extreme outliers. Compared to the fixed-power scenario in Fig. 7(c), this figure shows a performance degradation, reflected by an increased RMSE. Fig. 10(b) quantifies this increase in RMSE for a case involving 41 sources and a standard deviation of 2 dB.

TABLE I
COMPARISON OF ESTIMATION ACCURACY (RMSE) FOR ICNA WITH 2ND-, 3RD- AND 4TH-ORDER TWIN ARRAYS.

	Maximum Source Separation Angle ($\bar{\theta}_{\max}$, radians)				
$K = 35$	0.4	0.41	0.42	0.44	0.45
$\mathbb{P} \cup \mathbb{T}_2$	0.0012	0.0011	0.0013	0.0012	0.0013
$\mathbb{P} \cup \mathbb{T}_3$	0.0011	0.0010	0.0004	0.0013	0.0005
$\mathbb{P} \cup \mathbb{T}_4$	0.0004	0.0005	0.0018	0.0005	0.0006
$K = 50$	0.46	0.47	0.475	0.48	0.485
$\mathbb{P} \cup \mathbb{T}_2$	0.0009	0.0005	0.0008	0.0004	0.0011
$\mathbb{P} \cup \mathbb{T}_3$	0.0010	0.0004	0.0010	0.0008	0.0009
$\mathbb{P} \cup \mathbb{T}_4$	0.0008	0.0005	0.0006	0.0004	0.0005

*S*imulation parameters: $N = 13$, $\sigma_k^2 = -30$ dBm, $\sigma_n^2 = -40$ dBm, $T = 5000$.

Fig. 11(a) presents the spatial spectrum for the case where the angles of arrival of the CGSs are randomly generated from a mixed distribution. This distribution combines a Gaussian component (with zero mean and a standard deviation of $\bar{\theta}_{\max}/3$) to model clustered sources, and a uniform component (spanning $[-\bar{\theta}_{\max}, \bar{\theta}_{\max}]$) to model scattered sources. A minimum angular separation ($\bar{\theta}_{\min}$) of 0.025 radians is considered between all generated angles. The results show that the estimated angles closely align with the true directions of arrival. Fig. 11(b) further illustrates this accurate alignment for $K = 30$ CGSs with $\bar{\theta}_{\max} = 0.485$. This close alignment is also illustrated in Fig. 11(c), which involves a combination of randomly generated power levels and arrival angles.

TABLE II
COMPARISON OF ESTIMATION ACCURACY (RMSE) FOR ICNA WITH 2ND-, 3RD- AND 4TH-ORDER TWIN ARRAYS.

	Maximum Source Separation Angle ($\bar{\theta}_{\max}$, radians)				
$K = 50$	0.35	0.36	0.37	0.39	0.4
$\mathbb{P} \cup \mathbb{T}_2$	0.0003	0.0004	0.0007	0.0005	0.0005
$\mathbb{P} \cup \mathbb{T}_3$	0.0005	0.0005	0.0006	0.0006	0.0003
$\mathbb{P} \cup \mathbb{T}_4$	0.0003	0.0004	0.0003	0.0003	0.0003
$K = 60$	0.44	0.445	0.45	0.47	0.48
$\mathbb{P} \cup \mathbb{T}_2$	0.0004	0.0009	0.0008	0.0006	0.0009
$\mathbb{P} \cup \mathbb{T}_3$	0.0004	0.0009	0.0008	0.0009	0.0004
$\mathbb{P} \cup \mathbb{T}_4$	0.0004	0.0004	0.0004	0.0004	0.0005
$K = 65$	0.455	0.465	0.475	0.485	0.49
$\mathbb{P} \cup \mathbb{T}_2$	0.0005	0.0005	0.0007	0.0006	0.0006
$\mathbb{P} \cup \mathbb{T}_3$	0.0005	0.0008	0.0004	0.0007	0.0005
$\mathbb{P} \cup \mathbb{T}_4$	0.0003	0.0005	0.0005	0.0003	0.0004

*S*imulation parameters: $N = 15$, $\sigma_k^2 = -30$ dBm, $\sigma_n^2 = -40$ dBm, $T = 5000$.

VI. CONCLUDING REMARKS

This paper has introduced the twin array, a novel framework generating new spatial domains to enhance the DOF in array processing. The core of this approach involves applying the Hadamard product to the output vector of the physical sensor array to create a virtual array. Generalizing this operation to a Qth power produces a Qth-order expansion, reflecting a higher-order arrangement of the twin array. This arrangement provides a distinct cluster of virtual sensor locations, which

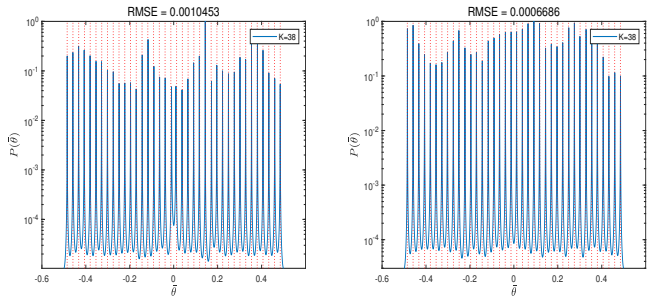

Fig. 9. MUSIC spectra computed from $\hat{\mathbf{R}}_{\mathbb{EE}}$ for a second-order DNA with its fourth-order twin, processing non-zero mean signals. **(a)** Estimation without mean removal. **(b)** Estimation after mean removal from the physical array output ($\mathbf{x}_{\mathbb{P}} - E[\mathbf{x}_{\mathbb{P}}]$). In this example, $|\mu_k|^2 = 0.00011281$ mWatt, $\sigma_k^2 = 0.001$ mWatt, and $\sigma_n^2 = 0.00011281$ mWatt. $N = 11$, $K = 38$ CGSs located at angles $\bar{\theta}_k = -0.485 + 0.97(k-1)/(K-1)$ for $k = 1, \ldots, K$, and $T = 5000$.

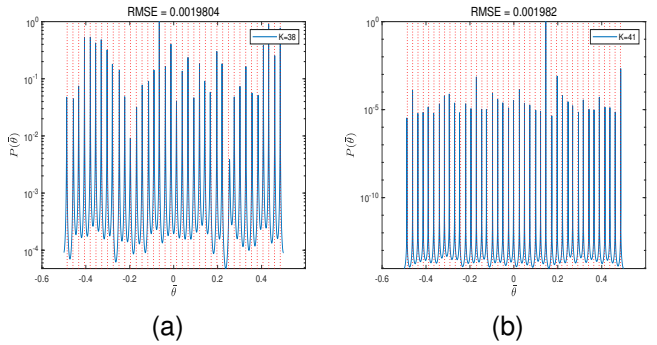

Fig. 10. $P(\bar{\theta})$ computed from $\hat{\mathbf{R}}_{\mathbb{EE}}$ for a second-order DNA with its fourth-order twin, under conditions of time-varying signal power. **(a)** Log-normal power distribution with a mean of -30 dBm and a standard deviation of 3 dB for $K = 38$ CGSs. **(b)** Log-normal power distribution with a mean of -30 dBm and a standard deviation of 2 dB for $K = 41$ CGSs. In this example, $N = 11$, $\bar{\theta}_k = -0.485 + 0.97(k-1)/(K-1)$ for $k = 1, \ldots, K$, $T = 5000$, and $\sigma_n^2 = -39.5$ dBm.

optimizes the original array DOF during the design phase. A key finding is that although these nonlinear expansions introduce higher-order moments, they do not dominate the signal power within the extended covariance matrix. This ensures the preservation of the matrix Gaussian properties, allowing standard second-order, subspace-based DOA estimation algorithms to be applied directly. By leveraging the enhanced uniform DOF offered by the physical-virtual array structure, these algorithms yield high-resolution spatial spectra. Furthermore, simulation results confirm that higher-order twin arrays achieve superior estimation accuracy compared to their lower-order counterparts.

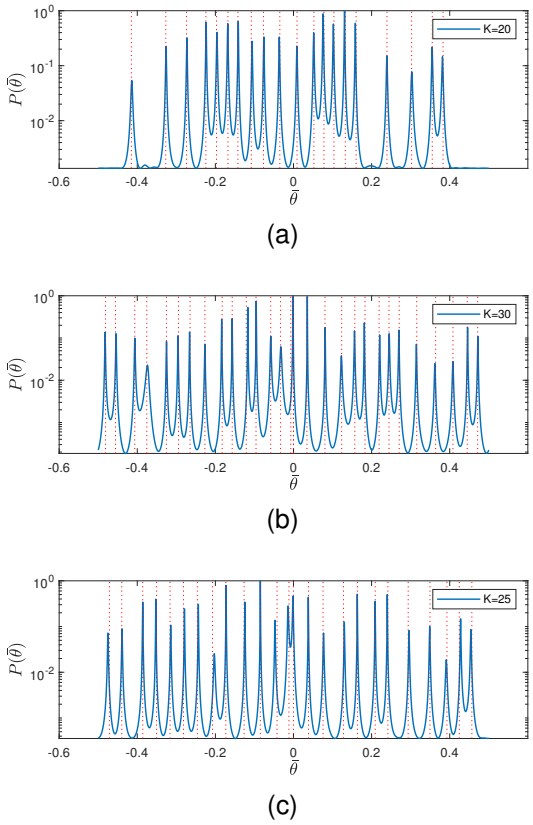

Fig. 11. $P(\bar{\theta})$ computed from $\hat{\mathbf{R}}_{\mathbb{EE}}$ for a second-order DNA with its fourth-order virtual twin, under random source arrivals following a Gaussian-uniform mixed distribution. The Gaussian component (70% of sources) has zero mean and a standard deviation of $\bar{\theta}_{\max}/3$. Common parameters: $N = 11$, $\sigma_k^2 = -30$ dBm, $\sigma_n^2 = -39.5$ dBm, and $T = 5000$. **(a)** $K = 20$ sources with $\bar{\theta}_{\max} = 0.45$ and $\bar{\theta}_{\min} = 0.025$. **(b)** $K = 30$ sources with $\bar{\theta}_{\max} = 0.485$ and $\bar{\theta}_{\min} = 0.025$. **(c)** $K = 25$ sources with a Log-Normal power distribution (mean of -30 dBm, standard deviation of 2 dB) and a Gaussian-uniform angle distribution ($\bar{\theta}_{\max} = 0.475$, $\bar{\theta}_{\min} = 0.03$). $\sigma_n^2 = -45$ dBm.

REFERENCES

[1] H. L. V. Trees, *Optimum Array Processing: Part IV of Detection Estimation and Modulation Theory*, Hoboken, NJ, USA: Wiley, 2004.

[2] P. Pal and P. P. Vaidyanathan, "Nested arrays: A novel approach to array processing with enhanced degrees of freedom," *IEEE Trans. on Signal Process.*, vol. 58, no. 8, pp. 4167–4181, Aug. 2010.

[3] P. P. Vaidyanathan and P. Pal, "Sparse sensing with co-prime samplers and arrays," *IEEE Trans. on Signal Process.*, vol. 59, no. 2, pp. 573–586, Feb. 2011.

[4] P. Pal and P. P. Vaidyanathan, "Coprime sampling and the music algorithm," *Dig. Signal Process. and Signal Process. Edu. Meeting (DSP/SPE)*, Sedona, AZ, USA, 2011, pp. 289–294.

[5] S. Qin, Y. D. Zhang and M. G. Amin, "Generalized coprime array configurations for direction-of-arrival estimation," *IEEE Trans. on Signal Process.*, vol. 63, no. 6, pp. 1377–1390, March15, 2015.

[6] C. -L. Liu and P. P. Vaidyanathan, "Super nested arrays: Linear sparse arrays with reduced mutual coupling—Part I: Fundamentals," *IEEE Trans. on Signal Process.*, vol. 64, no. 15, pp. 3997–4012, 1 Aug.1, 2016.

[7] C. -L. Liu and P. P. Vaidyanathan, "Super nested arrays: Linear sparse arrays with reduced mutual coupling—Part II: High-order extensions," *IEEE Trans. on Signal Process.*, vol. 64, no. 16, pp. 4203–4217, 15 Aug.15, 2016.

[8] W. Shi, S. A. Vorobyov and Y. Li, "ULA fitting for sparse array design," *IEEE Trans. on Signal Process.*, vol. 69, pp. 6431–6447, 2021.

[9] W. Shi, Y. Li and R. C. de Lamare, "Novel sparse array design based on the maximum inter-element spacing criterion", *IEEE Signal Process. Lett.*, vol. 29, pp. 1754–1758, 2022.

[10] N. Mohsen, A. Hawbani, M. Agrawal, S. Alsamhi and L. Zhao, "A new coprime-array-based configuration with augmented degrees of freedom and reduced mutual coupling," *Procs. of IEEE ICASSP*, Singapore, Singapore, 2022, pp. 5033–5037.

[11] J. Shi, F. Wen, Y. Liu, Z. Liu and P. Hu, "Enhanced and generalized coprime array for direction of arrival estimation," *IEEE Trans. on Aerospace and Electronic Systs.*, vol. 59, no. 2, pp. 1327–1339, April 2023.

[12] S. Wandale and K. Ichige, "xMISC: Improved sparse linear array via maximum inter-element spacing concept," *IEEE Signal Process. Lett.*, vol. 30, pp. 1327–1331, 2023.

[13] X. Wang, L. Zhao and Y. Jiang, "Super augmented nested arrays: A new sparse array for improved DOA estimation accuracy," *IEEE Signal Process. Lett.*, vol. 31, pp. 26–30, 2024.
[14] Ahmed M. A. Shaalan, J. Du and Y. -H. Tu, "Dilated nested arrays with more degrees of freedom and less mutual coupling—Part I: The fundamental geometry," *IEEE Trans. on Signal Process.*, vol. 70, pp. 2518–2531, 2022.
[15] Ahmed M. A. Shaalan and J. Du, "Super dilated nested arrays with ideal critical weights and increased degrees of freedom," *Procs. of IEEE ICASSP*, Rhodes Island, Greece, 2023, pp. 1–5.
[16] Ahmed M. A. Shaalan, and J. Du, "High-order dilated nested arrays with enhanced degree of freedom and reduced mutual coupling," *Dig. Signal Process.*, vol. 153, 104650, 2024.
[17] Z. Peng, Y. Ding, S. Ren, H. Wu and W. Wang, "Coprime nested arrays for DOA estimation: Exploiting the nesting property of coprime array," *IEEE Signal Process. Lett.*, vol. 29, pp. 444–448, 2022.
[18] H. Chen, H. Lin, W. Liu, Q. Wang, Q. Shen, and G. Wang, "Augmented multi-subarray dilated nested array with enhanced degrees of freedom and reduced mutual coupling," *IEEE Trans. on Signal Process.*, vol. 72, pp. 1387-1399, 2024.
[19] Y. Luo, F. Ning, and D. Peng, "SEDNA: An improved sparse array design for reduced mutual coupling and enhanced DOA estimation accuracy," *IEEE Signal Process. Lett.*, vol. 32, pp. 2838-2842, 2025.
[20] X. Wang, L. Zhao, Y. Jiang and Y. Wang, "An enhanced multi-ULA sparse array with improved DOA estimation performance," *IEEE Signal Process. Lett.*, vol. 32, pp. 2793-2797, 2025.
[21] A. H. Shaikh and X. Liu, "Super fragmented coprime arrays for DOA estimation," *IEEE Signal Process. Lett.*, vol. 32, pp. 1825-1829, 2025.
[22] X. Wang, Z. Chen, S. Ren and S. Cao, "DOA estimation based on the difference and sum coarray for coprime arrays," *Dig. Signal Process.*, vol. 69, pp. 22–31, Oct. 2017.
[23] P. Gupta and M. Agrawal, "Design and analysis of the sparse array for DOA estimation of noncircular signals," *IEEE Trans. on Signal Process.*, vol. 67, no. 2, pp. 460–473, Jan. 2019.
[24] W. Si, Z. Peng, C. Hou and F. Zeng, "Improved nested arrays with sum-difference coarray for DOA estimation," *IEEE Sensors J.*, vol. 19, no. 16, pp. 6986–6997, Aug. 2019.
[25] N. Mohsen, A. Hawbani, X. Wang, M. Agrawal and L. Zhao, "Optimized sparse nested arrays for DoA estimation of non-circular signals," *Signal Process.*, vol. 204, 2022.
[26] N. Mohsen, A. Hawbani, X. Wang, B. Bairrington, L. Zhao and S. Alsamhi, "New array designs for DoA estimation of non-circular signals with reduced mutual coupling," *IEEE Trans. on Vehicular Techn.*, vol. 72, no. 7, pp. 8313-8328, July 2023.
[27] Jiajie Li, Hua Chen, Wei Liu, Minghong Zhu, Qing Wang, Gang Wang, "Shifted super transformed nested array for DOA estimation of non-circular signals with increased uDOFs and reduced mutual coupling," *Signal Process.*, vol.221, pp.109508, 2024.
[28] Abdul Hayee Shaikh, Xiaoyu Dang, Daqing Huang, "Triad-displaced ULAs configuration for non-circular sources with larger continuous virtual aperture and enhanced degrees of freedom," *J. of Systs. Engineering and Electronics*, vol.35, no.1, pp.81–93, 2024.
[29] Lang Zhou, Zihao Feng, Kun Ye, Jie Qi, Shaohua Hong, "Design of relocating sparse nested arrays for DOA estimation of non-circular signals," *AEU - Int. J. of Electronics and Comm.*, vol.173, pp.154976, 2024.
[30] B. Porat and B. Friedlander, "Direction finding algorithms based on high-order statistics," *IEEE Trans. on Signal Process.*, vol. 39, no. 9, pp. 2016–2024, Sep. 1991.
[31] Q. Shen, W. Liu, W. Cui and S. Wu, "Extension of co-prime arrays based on the fourth-order difference co-array concept," *IEEE Signal Process. Lett.*, vol. 23, no. 5, pp. 615–619, May 2016.
[32] Baoping Wang, Junhao Zheng, "Cumulant-based DOA estimation of noncircular signals against unknown mutual coupling," *Sensors*, vol.20, no.3, pp.878, 2020.
[33] Z. Yang, Q. Shen, W. Liu, Y. C. Eldar and W. Cui, "Extended cantor arrays with hole-free fourth-order difference co-arrays," *Procs. IEEE Int. Symp. Circuits Syst.*, pp. 1–5, 2021.
[34] B. Dang and Y. Zhou, "The generalized compressed nested array for the construction of fourth-order difference co-array," *Circuits Syst. Signal Process.*, vol. 40, no. 12, pp. 6340–6353, Dec. 2021.
[35] Umesh Sharma, Monika Agrawal, "Third-order nested array: An optimal geometry for third-order cumulants based array processing," *IEEE Trans. on Signal Process.*, vol.71, pp.2849-2862, 2023.
[36] Z. Yang, Q. Shen, W. Liu, Y. C. Eldar and W. Cui, "High-order cumulants based sparse array design via fractal geometries—Part I: Structures and DOFs," *IEEE Trans. on Signal Process.*, vol. 71, pp. 327–342, 2023.
[37] Z. Yang, Q. Shen, W. Liu, Y. C. Eldar and W. Cui, "High-order cumulants based sparse array design via fractal geometries—Part II: Robustness and mutual coupling," *IEEE Trans. on Signal Process.*, 2023.
[38] H. Guo, H. Chen, W. Liu, S. Yang, C. Yuen and H. C. So, "Third-order sum-difference expansion: An array extension strategy based on third-order cumulants," *IEEE Trans. on Signal Process.*, vol. 73, pp. 2099-2109, 2025.
[39] H. Guo, H. Chen, S. Yang, W. Liu, C. Yuen and H. C. So, "A Third-order sparse array design scheme based on second-order sum-difference co-array analysis," *IEEE Trans. on Vehicular Techn.*, vol. 74, no. 4, pp. 6108-6120, 2025.
[40] H. Chen, H. Guo, W. Liu, Q. Shen, G. Wang and H. C. So, "Fourth-order sparse array design from a sum-difference co-array perspective," *IEEE Trans. on Signal Process.*, vol. 73, pp. 2243-2254, 2025.
[41] J. Mathews and G. L. Sicuranza, *Polynomial Signal Processing*, New York: Wiley, 2000.
[42] R. L. Graham, D. E. Knuth, and O. Patashnik, *Concrete Mathematics: A Foundation for Computer Science*, 2nd ed. Boston, MA, USA: Addison-Wesley Professional, 1994.
[43] C. -L. Liu and P. P. Vaidyanathan, "Remarks on the spatial smoothing step in coarray MUSIC," *IEEE Signal Process. Lett.*, vol. 22, no. 9, pp. 1438–1442, Sept. 2015, doi: 10.1109/LSP.2015.2409153.
[44] A. Barabell, "Improving the resolution performance of eigenstructure-based direction-finding algorithms," *Procs. of IEEE ICASSP*, Boston, MA, USA, 1983, pp. 336–339.
[45] R. Schmidt, "Multiple emitter location and signal parameter estimation," *IEEE Trans. on Ants. and Propagation*, vol. 34, no. 3, pp. 276–280, March 1986.